# Arctic Surface, Cloud, and Radiation Properties Based on the AVHRR Polar Pathfinder Dataset. Part I: Spatial and Temporal Characteristics

XUANJI WANG

*Cooperative Institute for Meteorological Satellite Studies, University of Wisconsin—Madison, Madison, Wisconsin*

JEFFREY R. KEY

*Office of Research and Applications, NOAA/NESDIS, Madison, Wisconsin*

(Manuscript received 1 February 2004, in final form 7 October 2004)

ABSTRACT

With broad spectral coverage and high spatial and temporal resolutions, satellite sensors can provide the data needed for the analysis of spatial and temporal variations of climate parameters in data-sparse regions such as the Arctic and Antarctic. The newly available Advanced Very High Resolution Radiometer (AVHRR) Polar Pathfinder (APP) dataset was used to retrieve cloud fraction, cloud optical depth, cloud particle phase and size, cloud-top pressure and temperature, surface skin temperature, surface broadband albedo, radiative fluxes, and cloud forcing over the Arctic Ocean and surrounding landmasses for the 18-yr period from 1982 to 1999. In the Arctic, Greenland is the coldest region with the highest surface albedo, while northeastern Russia has the highest surface temperature in summer. Arctic annual mean cloud coverage is about 70%, with the largest cloudiness occurring in September and the lowest cloudiness occurring in April. On annual average, Arctic cloud visible optical depth is about 5–6. Arctic precipitable water is near 0.2 cm in winter and 1.5 cm in summer. The largest downwelling shortwave radiative flux at the surface occurs in June; the largest upwelling shortwave radiative flux occurs in May. The largest downwelling and upwelling longwave radiative fluxes as well as the net all-wave radiative flux occur in July, with the largest loss of longwave radiation from the surface in April.

## 1. Introduction

The Arctic Ocean and its surrounding seas occupy an area of about 14 million km$^2$, most of which is ice covered in late winter. Many of the adjacent landmasses are low lying, which facilitate airmass exchanges with lower latitudes, except for the Greenland ice sheet, the ice-covered mountains of Ellesmere and Axel Heiberg islands in Canada, and the mountain ranges in Alaska and northeastern Siberia. The pack ice in the Arctic is a mixture of young and old floes that are highly variable in thickness and extent as a result of growth and decay along with ice dynamics. The interannual fluctuations and long-term trends in ice thickness and extent have important effects not only on Arctic climate but also on global climate change through complex feedback mechanisms.

It is well known that the global atmospheric circulation is basically driven by the equator-to-pole gradient between the low-latitude heat source and the polar heat sink (Barry et al. 1993). Numerous modeling studies have shown that the Arctic is one of the most sensitive regions on earth to global climate change (Manabe et al. 1992; Manabe and Stouffer 1994; Miller and Russell 2000; Meehl and Washington 1990) due to the positive feedback between surface temperature, surface albedo, and ice extent, known as the ice–albedo feedback (Curry et al. 1996). This theory has been confirmed by observational evidence, though records of Arctic climate change are brief and geographically sparse.

Currently, there are three major satellite-derived, multidecadal datasets that can be used to study the atmospheric characteristics of polar climate: the Advanced Very High Resolution Radiometer (AVHRR) Polar Pathfinder (APP; Fowler et al. 2000; Meier et al. 1997), the Television Infrared Observation Satellite

*Corresponding author address:* Dr. Xuanji Wang, Cooperative Institute for Meteorological Satellite Studies, University of Wisconsin—Madison, 1225 West Dayton Street, Madison, WI 53706.
E-mail: xuanjiw@ssec.wisc.edu

(TIROS) Operational Vertical Sounder Polar Pathfinder (TOVS Path-P) (Francis and Schweiger 1999), and the International Satellite Cloud Climatology Project (ISCCP) cloud dataset (Rossow et al. 1996). In addition, there are sea ice extent and snowmelt onset products derived from satellite passive-microwave multisensor data that provide a record of sufficient length for studying recent climate change (Cavalieri et al. 1999; Drobot and Anderson 2001). Each of these datasets covers a period of approximately 20 yr starting in the late 1970s. The standard APP dataset has clear-sky surface properties retrieved from satellite data with cloud mask information, the TOVS Path-P is made up of atmospheric temperature and humidity profiles, and the ISCCP dataset is the earliest satellite-based, long-term global dataset.

The purpose of this paper is to draw a more complete picture of Arctic climate by describing the temporal and spatial distributions of the climate components. First- and second-order statistics will be given for the surface, cloud, and radiation properties for the Arctic as a whole and for 18 subregions, by season and in the annual mean. Recent Arctic climate trends are discussed in Part II of this two-part paper (Wang and Key 2005).

## 2. Datasets, retrieved products, and validations

The primary dataset used in this study is a product of the APP project (Fowler et al. 2000; Meier et al. 1997). The APP dataset consists of twice-daily composites at a $5 \times 5$ km$^2$ pixel size over the period 1982–99. Key et al. (1997) investigated uncertainties of satellite-derived surface and cloud properties and surface radiation budget at the high latitudes and arrived at the conclusion that the accuracy in estimating radiation budgets from satellites is appropriate for a wide range of process studies at monthly time scales. The consistency of the products from different satellites over the period of 1982–99 was investigated by Wang and Key (2003), and they found no observable bias

The APP dataset was extended (hereinafter APP-x) for this study to include the retrievals of cloud fraction, cloud optical depth, cloud particle phase and size, cloud-top temperature and pressure, surface skin temperature, surface broadband albedo, and radiative fluxes, as well as cloud radiative effects ("cloud forcing"). For computational consideration, the original 5-km APP data were subsampled to 25 km by picking up the central pixel in a $5 \times 5$ pixel box. Retrievals were done with the Cloud and Surface Parameter Retrieval (CASPR) system (Key 2002a; Key et al. 2001), which was specifically designed for polar AVHRR daytime and nighttime data. All parameters are retrieved at all times, day or night. Radiative fluxes are calculated in CASPR using FluxNet (Key and Schweiger 1998), which is a neutral network version of a radiation transfer model called Streamer (Key 2002b). The atmospheric profiles of temperature and humidity from the National Centers for Environmental Prediction–National Center for Atmospheric Research (NCEP–NCAR) reanalysis dataset provided by the National Oceanic and Atmospheric Administration–Cooperative Institute for Research in Environmental Sciences (NOAA–CIRES) Climate Diagnostics Center in Boulder, Colorado, and the ISCCP Climatological Summary Product (D2) ozone dataset (Rossow et al. 1996) provided by the National Aeronautics and Space Administration (NASA) Langley Research Center were also used in CASPR retrieval process.

The daily APP-x composites are centered on a local solar time (LST) of 14:00 (high sun, but could be nighttime for some Arctic regions in winter). Approximately 90% of the pixels in each composite image are within 1 h of the target time; the largest time difference is 2 h before or after that target time. The Arctic region north of 60°N is of primary interest (Fig. 1). Figure 1 also shows the subregions for which results will be reported individually.

The extended products have been validated with the data collected during the Surface Heat Balance of the Arctic Ocean (SHEBA) field experiment in the western Arctic (Maslanik et al. 2001; Stroeve et al. 2001), and with the data from two Antarctic meteorological stations: South Pole and Neumayer (Pavolonis and Key 2003). The APP-x dataset was primarily compared with SHEBA ship measurements for the purpose of error estimation by averaging APP-x $5 \times 5$ pixel boxes ($25 \times 25$ km$^2$) centered on the SHEBA ship site. The SHEBA year started in the fall of 1997 and continued through the early fall of 1998. Table 1 gives satellite-derived quantities and the SHEBA ship measurements based on the averages of both local solar times of 14:00 and 04:00 over the period of 1997–98 for the surface skin temperature, surface broadband albedo, radiative fluxes, and cloud fraction.

Clouds are a very important component of the Arctic climate system (Wang and Key 2003). They affect Arctic climate by interacting with the atmosphere and highly reflective underlying surface through the absorption, emission, and scattering of radiation. Cloud detection and property estimation play a crucial role in the AVHRR retrievals of other climate parameters. Figure 2 shows an annual cycle of the total cloud fraction (cloud amount) based on the surface observations (Hahn 1995), the ISCCP D2 dataset, the TOVS Path-P

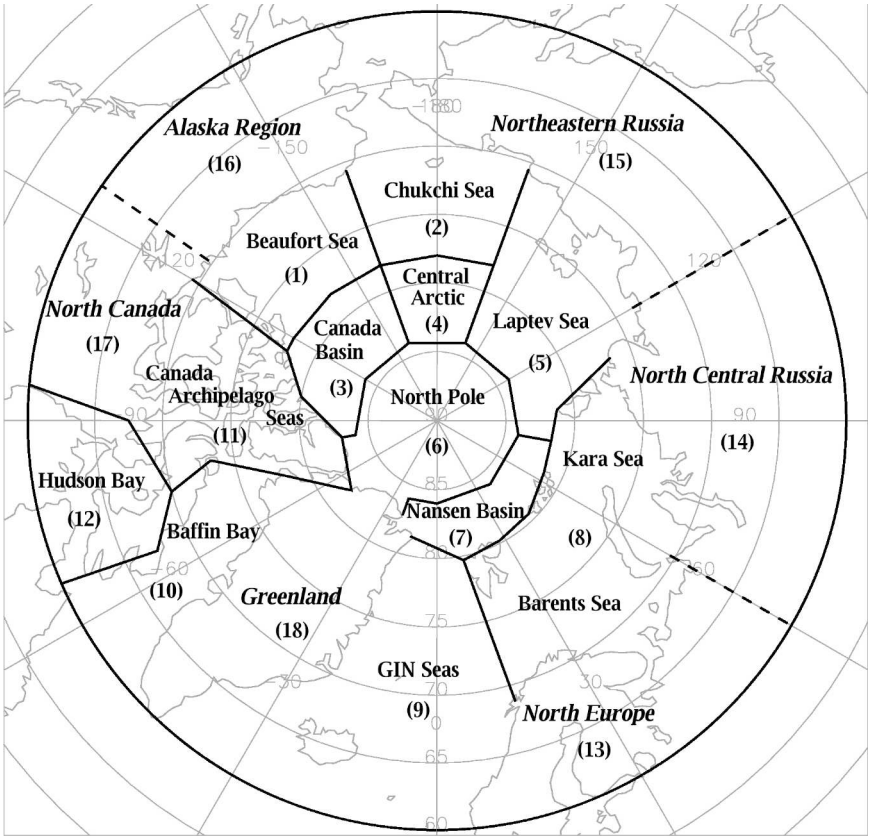


FIG. 1. Regional division of the Arctic north of 60°N.

dataset (Schweiger et al. 1999), and the APP-x dataset. The APP-x data in Fig. 2 were averaged over the period of 1982–91 from both local solar times of 14:00 and 04:00 for the comparisons with other studies. The surface-based climatology does not include clear-sky ice crystal precipitation. These low-level ice crystal clouds occur in winter about 20%–50% of the time and are often thick enough to have a significant radiative effect (Curry and Ebert 1992; Curry et al. 1996), which should be considered in satellite retrievals of other Arctic climate parameters. Overall, the APP-x dataset provides the best cloud fraction estimation among the other satellite retrievals regarding the comparisons and literature study.

Regarding cloud microphysical properties, Key and Intrieri (2000) reported that overall satellite retrievals of cloud particle phase have an accuracy of approximately 95% based on the comparison with the Depolarization and Backscatter Unattended Lidar (DABUL) observations during SHEBA. However,

TABLE 1. Comparisons of satellite-derived quantities and SHEBA ship measurements over the period of 1997–98.

| Quantity[a] | Bias[b] | Rmse[c] |
|---|---|---|
| Surface temperature | 0.20 K | 1.98 K |
| Surface broadband albedo | −0.05 (absolute) | 0.10 (absolute) |
| Downwelling shortwave radiation flux at the surface | 9.8 W $m^{-2}$ | 34.4 W $m^{-2}$ |
| Downwelling longwave radiation flux at the surface | 2.1 W $m^{-2}$ | 22.4 W $m^{-2}$ |
| Upwelling shortwave radiation flux at the surface | 4.4 W $m^{-2}$ | 26.6 W $m^{-2}$ |
| Upwelling longwave radiation flux at the surface | 1.9 W $m^{-2}$ | 9.4 W $m^{-2}$ |
| Cloud fraction | 0.14 (absolute) | 0.26 (absolute) |

[a] Satellite-derived quantities are for the 25 × 25 $km^2$ area centered on the SHEBA ship.
[b] Bias is defined as difference between satellite-derived quantities and SHEBA ship measurements.
[c] Rmse: root-mean-square error.

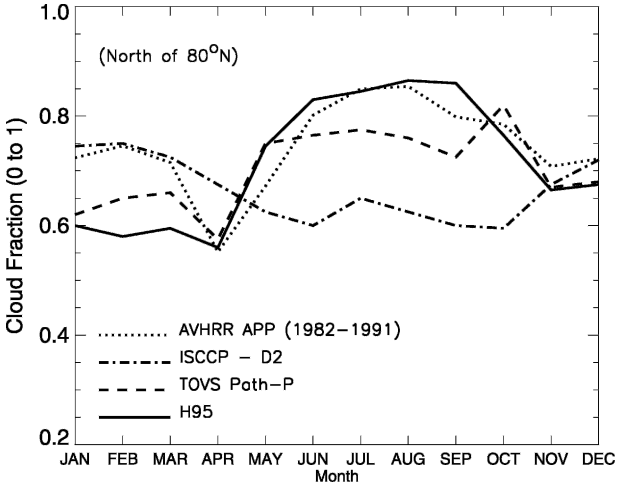


FIG. 2. Annual cycle of cloud fraction from surface-based observations (H95) and satellite retrievals (ISCCP D2, TOVS Path-P, and APP-x) for the Arctic region north of 80°N over the period 1982–91.

mixed-phase and multilayer clouds could not be identified in that study, so the overall accuracy will be less. Cloud particle size retrievals have not been examined in detail because of the lack of in situ measurements. Some comparisons have been done with aircraft observations during SHEBA, particularly with the Canadian National Research Council (NRC) Convair as reported by Gultepe et al. (2004). They showed that differences in the cloud particle effective radius between AVHRR-derived and aircraft observations are typically within 1–2 $\mu$m for water cloud–effective radii in the 8–10 $\mu$m range. For ice clouds, the differences are larger, on the order of 10 $\mu$m for particles with effective radii in the range of 30–100 $\mu$m.

## 3. Arctic climate characteristics

### *a. Surface skin temperature*

Surface skin temperature is a key climate parameter that encapsulates characteristics of a climate system. Surface air temperature has been recorded for decades at land-based and drifting ice meteorological stations, and a long time series over the Arctic Ocean is available in a recently compiled dataset based on Russian "North Pole" (NP) drifting station records, buoy measurements from the International Arctic Buoy Program (IABP), and coastal station observations (Martin et al. 1997; Martin and Munoz 1997). Serreze et al. (2000) pointed out that temperature trends derived from this dataset should be viewed cautiously because of the consistency problem in different data sources and instrument errors in different conditions. While a valuable source of information, the in situ data do not provide spatial details that can be obtained from satellite data.

Figure 3a shows the annual cycle of the APP-x surface skin temperatures averaged over 1982–99 for six Arctic regions: the Arctic region north of 60°N, the Arctic Ocean north of 60°N, the Arctic landmasses north of 60°N, Greenland, the North Pole, and the Greenland–Iceland–Norwegian (GIN) Seas. The entire Arctic region north of 60°N is divided into 18 subregions for a detailed study of those subregions (Groves and Francis 2002). The retrieved all-sky surface skin temperature on a local solar time of 14:00 should be close to the daily maximum surface temperature. The surface temperature reaches a maximum value of about 10°C in July and a minimum value of –25°C in January.

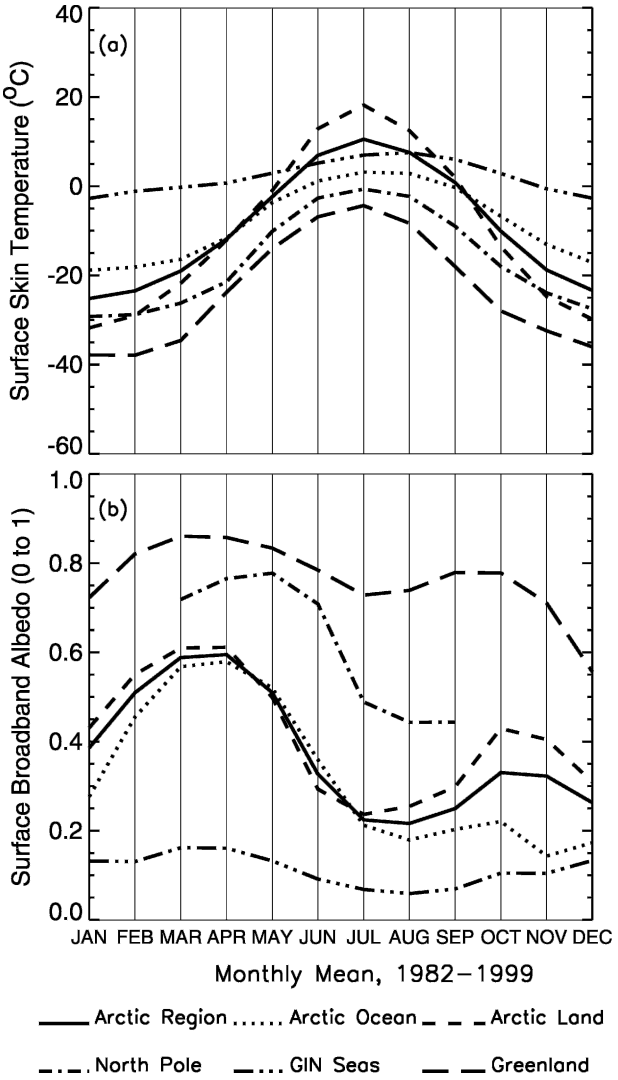


FIG. 3. Annual cycles of surface skin temperatures and surface broadband albedos for six Arctic regions averaged over the period 1982–99 on a local solar time of 14:00.

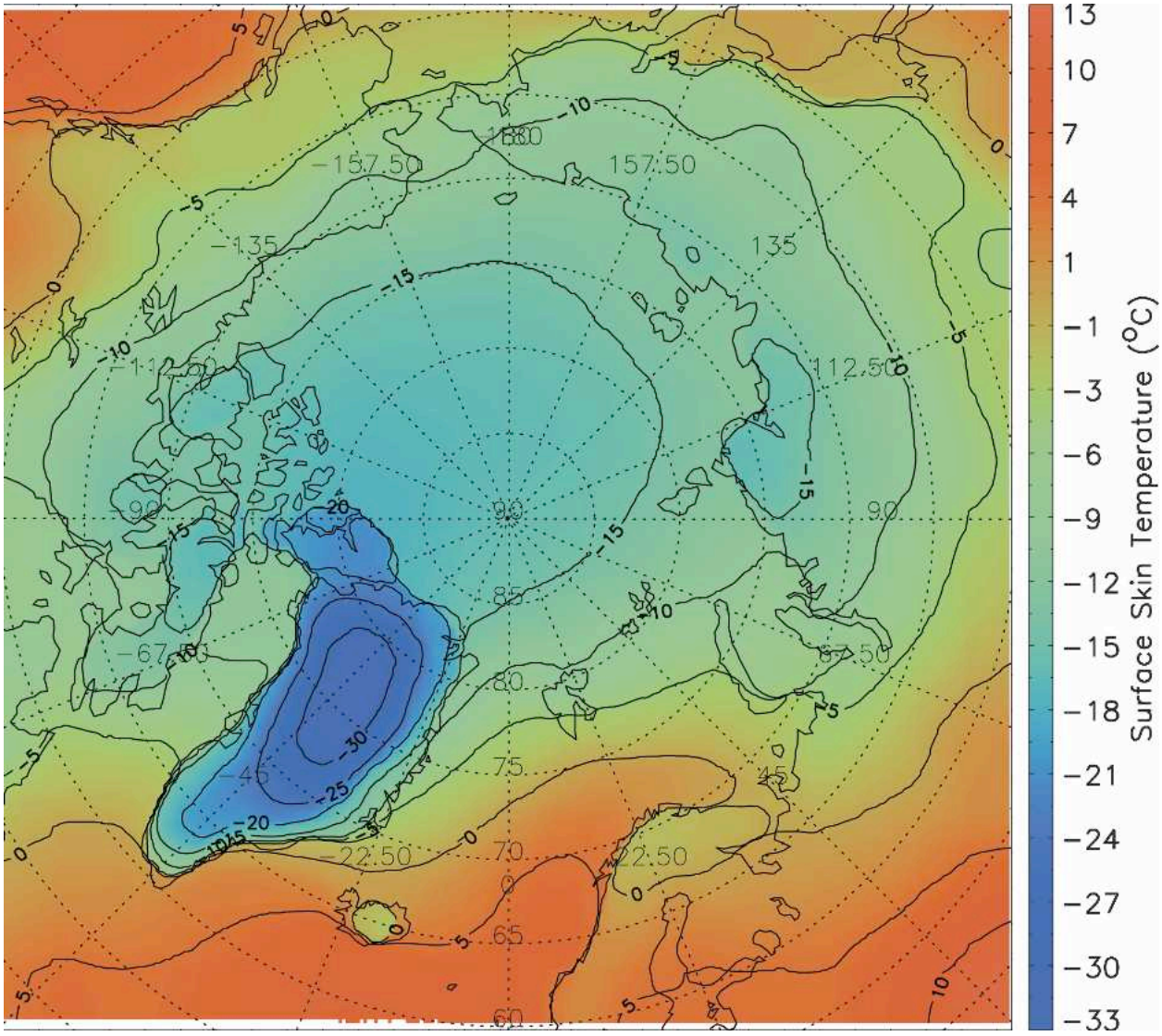


FIG. 4. Spatial distribution of annual mean surface skin temperature (°C) averaged over the period 1982–99 on a local solar time of 14:00.

For the Arctic Ocean, the surface temperature is close to the freezing point (0°C) in July and about –19°C in January. For the Arctic landmasses including Greenland, the surface temperature reaches about 19°C in July as a maximum and reaches a minimum of –32°C in January. On an annual scale, the surface temperature range is the largest over the landmasses and the smallest in the Arctic Ocean as a result of large heat capacity of water.

Figure 4 shows the spatial distribution of the annual mean surface temperature. Central Greenland has the lowest surface temperature, as low as –30°C, and the Arctic Ocean and coastal areas are colder than the landmasses. In winter the surface temperature of the Arctic Ocean is overall higher than that of the Arctic surrounding landmasses, but Greenland still has the lowest surface temperature, as low as –45°C (not shown). In summer the surface temperature of the Arctic Ocean is lower than that of the Arctic surrounding landmasses, with Greenland once again exhibiting the lowest temperature (–10°C).

The seasonal values of the 18 parameters averaged over the period 1982–99 are listed in Table 2 for the Arctic subregions along with the average results for the Arctic region north of 60°N, the Arctic Ocean north of 60°N, and the Arctic landmasses north of 60°N. The names and representative ID numbers of the 21 Arctic subregions are listed in Table 3. The names and

TABLE 2. Seasonal values of the 18 climate parameters for the 21 Arctic subregions.

| PID[a] name | Season | Region ID[b] 1 | Region ID 2 | Region ID 3 | Region ID 4 | Region ID 5 | Region ID 6 | Region ID 7 |
|---|---|---|---|---|---|---|---|---|
| $T_s$ | Winter | 246.03 | 248.48 | 242.26 | 244.39 | 246.51 | 244.51 | 251.00 |
| | Spring | 256.58 | 257.46 | 252.80 | 253.43 | 255.40 | 253.84 | 258.61 |
| | Summer | 273.18 | 273.59 | 271.27 | 271.44 | 273.07 | 271.24 | 272.91 |
| | Autumn | 259.43 | 262.18 | 255.32 | 256.63 | 260.46 | 256.14 | 261.30 |
| $\alpha_s$ | Winter | 0.71 | 0.71 | 9999.00[c] | 9999.00 | 0.68 | 9999.00 | 9999.00 |
| | Spring | 0.79 | 0.78 | 0.78 | 0.78 | 0.77 | 0.75 | 0.71 |
| | Summer | 0.40 | 0.35 | 0.58 | 0.55 | 0.36 | 0.55 | 0.34 |
| | Autumn | 0.47 | 0.35 | 0.57 | 0.52 | 0.28 | 0.44 | 0.26 |
| $R_e$ | Winter | 26.87 | 26.10 | 21.90 | 21.50 | 23.26 | 18.93 | 19.28 |
| | Spring | 19.55 | 18.32 | 21.77 | 21.90 | 20.52 | 19.46 | 17.34 |
| | Summer | 12.47 | 11.47 | 10.89 | 10.47 | 10.97 | 9.18 | 9.63 |
| | Autumn | 21.50 | 19.13 | 20.49 | 19.66 | 18.40 | 17.58 | 17.41 |
| $\tau_c$ | Winter | 3.40 | 4.11 | 2.42 | 2.95 | 3.74 | 3.78 | 5.46 |
| | Spring | 3.99 | 4.02 | 5.60 | 5.80 | 5.54 | 10.03 | 8.53 |
| | Summer | 2.28 | 3.24 | 4.09 | 4.34 | 5.32 | 9.54 | 9.28 |
| | Autumn | 4.27 | 4.89 | 4.22 | 4.30 | 5.04 | 4.46 | 5.91 |
| $\phi_c$ | Winter | 0.65 | 0.67 | 0.55 | 0.55 | 0.62 | 0.55 | 0.60 |
| | Spring | 0.59 | 0.59 | 0.65 | 0.64 | 0.64 | 0.61 | 0.61 |
| | Summer | 0.46 | 0.45 | 0.48 | 0.46 | 0.46 | 0.36 | 0.39 |
| | Autumn | 0.65 | 0.63 | 0.61 | 0.60 | 0.63 | 0.53 | 0.60 |
| $T_c$ | Winter | 242.44 | 243.82 | 238.46 | 240.14 | 240.90 | 238.34 | 241.96 |
| | Spring | 251.78 | 252.14 | 246.85 | 248.17 | 249.13 | 245.96 | 249.57 |
| | Summer | 264.52 | 264.78 | 262.48 | 262.68 | 264.00 | 262.33 | 264.01 |
| | Autumn | 252.68 | 254.21 | 248.26 | 249.78 | 252.11 | 247.92 | 251.07 |
| $P_c$ | Winter | 644.61 | 648.55 | 590.06 | 598.47 | 638.01 | 589.71 | 653.86 |
| | Spring | 697.48 | 699.60 | 656.90 | 669.10 | 685.37 | 645.90 | 693.11 |
| | Summer | 690.80 | 689.61 | 701.56 | 698.94 | 698.24 | 705.58 | 722.93 |
| | Autumn | 690.02 | 703.30 | 642.94 | 658.15 | 700.87 | 644.64 | 677.66 |
| PW | Winter | 0.14 | 0.17 | 0.09 | 0.12 | 0.15 | 0.10 | 0.15 |
| | Spring | 0.31 | 0.35 | 0.24 | 0.26 | 0.30 | 0.24 | 0.29 |
| | Summer | 1.15 | 1.21 | 0.99 | 1.03 | 1.13 | 0.96 | 1.00 |
| | Autumn | 0.41 | 0.46 | 0.32 | 0.35 | 0.42 | 0.32 | 0.40 |
| $SW\downarrow_{srf}$ | Winter | 12.05 | 16.36 | 0.00 | 0.00 | 1.98 | 0.00 | 0.00 |
| | Spring | 396.42 | 409.14 | 266.43 | 267.70 | 310.54 | 149.58 | 193.32 |
| | Summer | 515.04 | 487.67 | 376.33 | 363.89 | 354.83 | 227.34 | 215.92 |
| | Autumn | 83.21 | 80.74 | 37.60 | 36.82 | 45.85 | 24.44 | 24.09 |
| $LW\downarrow_{srf}$ | Winter | 169.58 | 175.68 | 154.91 | 162.44 | 170.52 | 171.12 | 195.93 |
| | Spring | 192.83 | 195.18 | 189.31 | 189.62 | 192.59 | 207.90 | 220.21 |
| | Summer | 269.79 | 282.99 | 278.40 | 282.58 | 293.06 | 291.23 | 299.56 |
| | Autumn | 226.71 | 240.12 | 211.92 | 215.71 | 232.57 | 218.95 | 237.64 |
| $SW\uparrow_{srf}$ | Winter | 8.66 | 11.77 | 0.00 | 0.00 | 1.43 | 0.00 | 0.00 |
| | Spring | 293.24 | 300.23 | 200.17 | 200.12 | 229.58 | 108.39 | 131.43 |
| | Summer | 191.94 | 168.17 | 215.40 | 198.87 | 124.65 | 126.35 | 74.92 |
| | Autumn | 34.15 | 23.18 | 21.95 | 19.57 | 9.14 | 11.46 | 5.69 |
| $LW\uparrow_{srf}$ | Winter | 207.56 | 215.46 | 194.96 | 202.04 | 208.94 | 202.55 | 224.77 |
| | Spring | 246.25 | 249.55 | 232.24 | 234.43 | 241.79 | 235.91 | 253.02 |
| | Summer | 315.24 | 317.21 | 306.74 | 307.51 | 315.13 | 306.88 | 314.65 |
| | Autumn | 259.20 | 270.17 | 241.13 | 245.83 | 263.02 | 246.23 | 263.88 |
| $SW\downarrow_{toa}$ | Winter | 16.39 | 22.98 | 0.00 | 0.00 | 4.00 | 0.00 | 0.00 |
| | Spring | 525.29 | 541.48 | 387.14 | 390.03 | 441.43 | 287.69 | 354.21 |
| | Summer | 744.18 | 761.60 | 617.75 | 623.81 | 674.90 | 526.65 | 591.46 |
| | Autumn | 166.02 | 181.51 | 83.36 | 86.55 | 121.65 | 50.44 | 73.80 |
| $SW\uparrow_{toa}$ | Winter | 16.32 | 21.42 | 0.00 | 0.00 | 2.94 | 0.00 | 0.00 |
| | Spring | 349.20 | 357.24 | 278.38 | 278.90 | 302.35 | 199.35 | 253.90 |
| | Summer | 315.97 | 325.95 | 354.61 | 353.29 | 335.67 | 335.91 | 350.39 |
| | Autumn | 98.38 | 100.99 | 56.62 | 56.66 | 69.45 | 40.33 | 45.43 |
| $LW\uparrow_{toa}$ | Winter | 172.63 | 176.21 | 165.34 | 169.11 | 171.37 | 164.97 | 172.31 |
| | Spring | 191.40 | 192.40 | 182.70 | 184.71 | 187.73 | 181.12 | 187.36 |
| | Summer | 226.41 | 225.85 | 219.96 | 220.01 | 222.56 | 218.44 | 220.41 |
| | Autumn | 197.51 | 200.65 | 187.60 | 190.11 | 195.79 | 187.58 | 192.64 |

TABLE 2. (*Continued*)

| PID name | Season | Region ID 1 | Region ID 2 | Region ID 3 | Region ID 4 | Region ID 5 | Region ID 6 | Region ID 7 |
|---|---|---|---|---|---|---|---|---|
| $CF_S$ | Winter | −0.61 | −0.74 | 0.00 | 0.00 | −0.05 | 0.00 | 0.00 |
| | Spring | −4.71 | −4.86 | −8.24 | −8.01 | −6.50 | −13.00 | −21.26 |
| | Summer | −37.58 | −68.53 | −40.91 | −49.65 | −97.76 | −68.25 | −138.91 |
| | Autumn | −18.40 | −29.58 | −7.65 | −9.32 | −23.95 | −6.65 | −14.46 |
| $CF_L$ | Winter | 23.51 | 23.51 | 17.26 | 20.21 | 23.17 | 28.89 | 39.35 |
| | Spring | 14.15 | 14.36 | 24.18 | 22.53 | 18.70 | 42.11 | 41.79 |
| | Summer | 31.14 | 42.66 | 49.75 | 52.93 | 55.97 | 63.67 | 66.27 |
| | Autumn | 41.95 | 47.92 | 41.60 | 41.55 | 46.15 | 45.25 | 51.51 |
| $A_c$ | Winter | 0.65 | 0.63 | 0.65 | 0.65 | 0.65 | 0.71 | 0.74 |
| | Spring | 0.53 | 0.52 | 0.59 | 0.56 | 0.54 | 0.71 | 0.68 |
| | Summer | 0.74 | 0.79 | 0.81 | 0.84 | 0.84 | 0.87 | 0.90 |
| | Autumn | 0.77 | 0.79 | 0.77 | 0.76 | 0.77 | 0.79 | 0.80 |
| PID name | Season | Region ID 8 | Region ID 9 | Region ID 10 | Region ID 11 | Region ID 12 | Region ID 13 | Region ID 14 |
| $T_s$ | Winter | 258.80 | 270.88 | 256.54 | 244.40 | 252.35 | 255.90 | 242.30 |
| | Spring | 265.76 | 274.23 | 263.25 | 255.52 | 262.24 | 273.62 | 262.62 |
| | Summer | 276.27 | 279.68 | 275.45 | 273.72 | 275.45 | 292.96 | 291.64 |
| | Autumn | 269.86 | 275.88 | 270.27 | 260.93 | 269.48 | 271.93 | 262.20 |
| $\alpha_s$ | Winter | 0.36 | 0.14 | 0.53 | 0.73 | 0.64 | 0.32 | 0.47 |
| | Spring | 0.46 | 0.15 | 0.55 | 0.80 | 0.69 | 0.28 | 0.51 |
| | Summer | 0.13 | 0.07 | 0.11 | 0.31 | 0.14 | 0.15 | 0.18 |
| | Autumn | 0.11 | 0.09 | 0.07 | 0.28 | 0.10 | 0.22 | 0.31 |
| $R_e$ | Winter | 18.40 | 15.28 | 22.46 | 25.80 | 30.06 | 18.40 | 25.17 |
| | Spring | 13.13 | 11.63 | 13.78 | 21.02 | 13.73 | 10.38 | 14.80 |
| | Summer | 10.47 | 10.69 | 11.09 | 11.97 | 11.66 | 8.21 | 8.39 |
| | Autumn | 15.08 | 15.61 | 15.41 | 19.74 | 15.04 | 13.12 | 15.87 |
| $\tau_c$ | Winter | 5.77 | 7.11 | 5.86 | 3.74 | 5.54 | 5.58 | 4.55 |
| | Spring | 6.06 | 6.51 | 5.00 | 5.11 | 3.93 | 5.87 | 4.84 |
| | Summer | 6.48 | 6.57 | 5.46 | 3.51 | 4.57 | 5.92 | 5.48 |
| | Autumn | 6.39 | 6.90 | 6.03 | 5.28 | 5.76 | 6.06 | 5.16 |
| $\phi_c$ | Winter | 0.65 | 0.64 | 0.76 | 0.67 | 0.86 | 0.70 | 0.78 |
| | Spring | 0.53 | 0.47 | 0.58 | 0.69 | 0.58 | 0.48 | 0.64 |
| | Summer | 0.39 | 0.36 | 0.42 | 0.45 | 0.42 | 0.26 | 0.28 |
| | Autumn | 0.58 | 0.58 | 0.62 | 0.66 | 0.60 | 0.49 | 0.57 |
| $T_c$ | Winter | 248.86 | 253.46 | 245.50 | 238.85 | 244.30 | 249.40 | 240.77 |
| | Spring | 254.59 | 257.77 | 252.80 | 248.76 | 253.38 | 258.73 | 253.63 |
| | Summer | 265.60 | 266.90 | 263.74 | 263.15 | 264.01 | 264.92 | 263.98 |
| | Autumn | 257.08 | 259.02 | 255.79 | 251.73 | 256.51 | 258.22 | 252.38 |
| $P_c$ | Winter | 731.61 | 680.18 | 741.07 | 654.86 | 793.72 | 620.11 | 580.30 |
| | Spring | 728.33 | 702.59 | 729.77 | 689.25 | 736.29 | 697.77 | 694.43 |
| | Summer | 710.18 | 707.36 | 687.48 | 696.34 | 670.20 | 644.26 | 640.35 |
| | Autumn | 729.43 | 673.37 | 702.71 | 698.67 | 706.86 | 646.66 | 637.91 |
| PW | Winter | 0.28 | 0.55 | 0.16 | 0.10 | 0.12 | 0.44 | 0.20 |
| | Spring | 0.43 | 0.67 | 0.33 | 0.25 | 0.33 | 0.74 | 0.47 |
| | Summer | 1.21 | 1.31 | 1.04 | 1.00 | 1.23 | 1.79 | 1.69 |
| | Autumn | 0.63 | 0.88 | 0.53 | 0.38 | 0.59 | 0.95 | 0.62 |
| $SW\downarrow_{srf}$ | Winter | 5.63 | 25.72 | 39.48 | 12.65 | 85.50 | 59.82 | 53.30 |
| | Spring | 265.22 | 278.32 | 391.11 | 390.54 | 516.04 | 362.69 | 418.37 |
| | Summer | 323.61 | 366.92 | 438.76 | 469.73 | 580.80 | 522.70 | 532.66 |
| | Autumn | 52.98 | 95.68 | 105.28 | 66.96 | 130.79 | 137.48 | 134.78 |
| $LW\downarrow_{srf}$ | Winter | 225.23 | 271.43 | 210.55 | 168.00 | 187.63 | 211.88 | 161.67 |
| | Spring | 241.81 | 281.27 | 221.35 | 189.81 | 214.29 | 277.54 | 223.20 |
| | Summer | 306.46 | 319.80 | 295.04 | 276.64 | 286.48 | 359.09 | 349.74 |
| | Autumn | 272.36 | 295.78 | 269.08 | 235.37 | 271.69 | 278.86 | 236.56 |
| $SW\uparrow_{srf}$ | Winter | 1.98 | 1.90 | 18.02 | 9.64 | 58.52 | 17.97 | 20.49 |
| | Spring | 121.78 | 37.85 | 198.86 | 295.74 | 335.97 | 87.35 | 195.81 |
| | Summer | 40.69 | 24.30 | 48.22 | 143.32 | 78.00 | 78.01 | 91.74 |
| | Autumn | 2.74 | 4.72 | 4.61 | 12.40 | 7.25 | 24.79 | 33.26 |

TABLE 2. (*Continued*)

| PID name | Season | Region ID 8 | Region ID 9 | Region ID 10 | Region ID 11 | Region ID 12 | Region ID 13 | Region ID 14 |
|---|---|---|---|---|---|---|---|---|
| $LW\uparrow_{srf}$ | Winter | 255.46 | 305.77 | 244.38 | 202.10 | 223.60 | 244.76 | 198.62 |
| | Spring | 282.69 | 320.35 | 271.56 | 242.08 | 267.43 | 319.11 | 271.50 |
| | Summer | 330.66 | 347.51 | 326.50 | 317.90 | 326.17 | 416.79 | 409.75 |
| | Autumn | 301.96 | 329.26 | 303.38 | 264.99 | 301.89 | 315.37 | 275.23 |
| $SW\downarrow_{toa}$ | Winter | 12.12 | 69.42 | 72.66 | 18.46 | 118.54 | 102.34 | 78.97 |
| | Spring | 496.67 | 617.64 | 625.77 | 519.74 | 698.24 | 680.74 | 642.66 |
| | Summer | 723.16 | 828.43 | 834.47 | 739.96 | 897.27 | 884.98 | 853.16 |
| | Autumn | 152.55 | 251.32 | 256.20 | 164.33 | 322.31 | 307.46 | 274.41 |
| $SW\uparrow_{toa}$ | Winter | 9.95 | 52.98 | 62.02 | 17.16 | 109.67 | 70.74 | 55.29 |
| | Spring | 277.51 | 261.59 | 346.55 | 355.26 | 424.41 | 293.57 | 326.77 |
| | Summer | 301.62 | 311.37 | 288.17 | 307.10 | 252.83 | 287.76 | 277.95 |
| | Autumn | 79.01 | 118.46 | 115.69 | 88.43 | 145.52 | 153.69 | 139.73 |
| $LW\uparrow_{toa}$ | Winter | 187.27 | 200.24 | 179.75 | 167.14 | 176.02 | 190.33 | 170.84 |
| | Spring | 199.29 | 209.78 | 196.19 | 187.36 | 197.42 | 212.86 | 198.93 |
| | Summer | 226.88 | 231.24 | 225.51 | 224.58 | 229.59 | 240.45 | 241.23 |
| | Autumn | 208.50 | 217.56 | 207.94 | 195.77 | 208.43 | 215.63 | 200.33 |
| $CF_S$ | Winter | −1.84 | −21.31 | −12.73 | −0.70 | −7.44 | −9.49 | −2.75 |
| | Spring | −66.44 | −151.89 | −57.11 | −5.36 | −17.49 | −102.87 | −41.91 |
| | Summer | −187.35 | −248.89 | −181.77 | −73.28 | −101.56 | −126.10 | −91.22 |
| | Autumn | −38.63 | −65.16 | −63.22 | −32.98 | −81.80 | −50.91 | −34.39 |
| $CF_L$ | Winter | 47.11 | 57.08 | 44.42 | 27.71 | 34.75 | 33.10 | 17.24 |
| | Spring | 41.84 | 53.54 | 30.80 | 15.90 | 23.17 | 47.07 | 26.61 |
| | Summer | 57.04 | 56.42 | 51.76 | 39.80 | 37.83 | 36.71 | 32.95 |
| | Autumn | 56.77 | 56.13 | 55.06 | 49.67 | 57.97 | 47.12 | 35.51 |
| $A_c$ | Winter | 0.79 | 0.86 | 0.76 | 0.68 | 0.70 | 0.64 | 0.52 |
| | Spring | 0.71 | 0.81 | 0.65 | 0.54 | 0.62 | 0.74 | 0.58 |
| | Summer | 0.83 | 0.84 | 0.78 | 0.75 | 0.69 | 0.70 | 0.67 |
| | Autumn | 0.83 | 0.83 | 0.81 | 0.79 | 0.85 | 0.73 | 0.65 |

| PID name | Season | Region ID 15 | Region ID 16 | Region ID 17 | Region ID 18 | Region ID 19 | Region ID 20 | Region ID 21 |
|---|---|---|---|---|---|---|---|---|
| $T_s$ | Winter | 238.20 | 247.82 | 239.75 | 235.83 | 249.05 | 255.02 | 242.89 |
| | Spring | 260.89 | 266.74 | 256.68 | 248.97 | 262.02 | 262.53 | 261.50 |
| | Summer | 293.02 | 291.74 | 285.32 | 266.60 | 281.45 | 275.48 | 287.62 |
| | Autumn | 260.17 | 264.02 | 259.88 | 246.97 | 263.76 | 266.40 | 261.03 |
| $\alpha_s$ | Winter | 0.54 | 0.44 | 0.70 | 0.81 | 0.50 | 0.44 | 0.53 |
| | Spring | 0.58 | 0.47 | 0.73 | 0.85 | 0.56 | 0.56 | 0.57 |
| | Summer | 0.16 | 0.17 | 0.25 | 0.75 | 0.26 | 0.25 | 0.26 |
| | Autumn | 0.33 | 0.26 | 0.47 | 0.77 | 0.31 | 0.23 | 0.39 |
| $R_e$ | Winter | 29.57 | 25.28 | 25.38 | 24.89 | 22.91 | 20.89 | 25.00 |
| | Spring | 17.99 | 16.82 | 16.50 | 21.79 | 16.14 | 16.06 | 16.22 |
| | Summer | 8.65 | 9.42 | 9.97 | 12.22 | 10.06 | 10.78 | 9.33 |
| | Autumn | 18.09 | 17.57 | 17.09 | 21.41 | 17.04 | 17.05 | 17.03 |
| $\tau_c$ | Winter | 3.81 | 5.36 | 3.91 | 4.52 | 4.81 | 5.06 | 4.55 |
| | Spring | 4.76 | 4.10 | 5.00 | 7.12 | 5.55 | 5.86 | 5.23 |
| | Summer | 5.03 | 4.70 | 4.22 | 5.52 | 5.44 | 5.71 | 5.17 |
| | Autumn | 4.70 | 5.01 | 4.60 | 6.05 | 5.44 | 5.67 | 5.21 |
| $\phi_c$ | Winter | 0.79 | 0.78 | 0.69 | 0.72 | 0.70 | 0.65 | 0.75 |
| | Spring | 0.69 | 0.62 | 0.59 | 0.81 | 0.60 | 0.57 | 0.64 |
| | Summer | 0.30 | 0.33 | 0.34 | 0.48 | 0.36 | 0.40 | 0.32 |
| | Autumn | 0.61 | 0.64 | 0.57 | 0.66 | 0.59 | 0.60 | 0.59 |
| $T_c$ | Winter | 239.52 | 244.54 | 240.85 | 235.65 | 243.65 | 245.65 | 241.58 |
| | Spring | 253.46 | 255.87 | 252.94 | 246.32 | 253.08 | 252.69 | 253.49 |
| | Summer | 262.86 | 261.81 | 263.06 | 258.09 | 263.75 | 264.77 | 262.70 |
| | Autumn | 251.35 | 252.47 | 252.65 | 245.28 | 253.43 | 254.69 | 252.14 |
| $P_c$ | Winter | 596.03 | 575.11 | 625.31 | 514.22 | 630.83 | 672.21 | 588.14 |
| | Spring | 709.71 | 685.06 | 702.35 | 605.07 | 693.06 | 699.84 | 686.08 |
| | Summer | 621.86 | 608.34 | 659.21 | 617.39 | 666.62 | 698.23 | 633.99 |
| | Autumn | 636.91 | 607.27 | 649.31 | 553.96 | 658.40 | 689.34 | 626.48 |

TABLE 2. (*Continued*)

| PID name | Season | Region ID 15 | Region ID 16 | Region ID 17 | Region ID 18 | Region ID 19 | Region ID 20 | Region ID 21 |
|---|---|---|---|---|---|---|---|---|
| PW | Winter | 0.16 | 0.30 | 0.15 | 0.06 | 0.23 | 0.26 | 0.21 |
| | Spring | 0.41 | 0.51 | 0.37 | 0.15 | 0.43 | 0.41 | 0.44 |
| | Summer | 1.57 | 1.46 | 1.27 | 0.54 | 1.31 | 1.19 | 1.43 |
| | Autumn | 0.52 | 0.61 | 0.53 | 0.17 | 0.57 | 0.57 | 0.57 |
| $SW\downarrow_{srf}$ | Winter | 62.55 | 64.00 | 58.79 | 24.09 | 37.21 | 20.16 | 54.81 |
| | Spring | 466.49 | 444.31 | 490.34 | 429.13 | 376.54 | 317.77 | 437.19 |
| | Summer | 561.26 | 549.86 | 566.99 | 602.31 | 470.27 | 390.43 | 552.67 |
| | Autumn | 150.09 | 149.03 | 141.96 | 121.82 | 106.17 | 74.12 | 139.24 |
| $LW\downarrow_{srf}$ | Winter | 148.87 | 183.27 | 148.03 | 141.36 | 186.00 | 207.07 | 164.27 |
| | Spring | 212.20 | 239.43 | 194.31 | 159.06 | 221.93 | 226.55 | 217.16 |
| | Summer | 351.21 | 346.89 | 317.48 | 226.10 | 313.26 | 298.05 | 328.96 |
| | Autumn | 225.46 | 241.10 | 222.74 | 165.10 | 243.52 | 257.26 | 229.35 |
| $SW\uparrow_{srf}$ | Winter | 33.00 | 26.19 | 37.84 | 18.04 | 16.92 | 8.19 | 25.93 |
| | Spring | 252.36 | 185.15 | 333.61 | 343.23 | 201.31 | 169.71 | 233.91 |
| | Summer | 90.87 | 91.67 | 128.96 | 434.15 | 115.79 | 91.58 | 140.77 |
| | Autumn | 38.50 | 31.56 | 48.98 | 87.49 | 26.31 | 10.50 | 42.61 |
| $LW\uparrow_{srf}$ | Winter | 185.95 | 215.85 | 188.55 | 176.74 | 221.44 | 241.76 | 200.47 |
| | Spring | 264.30 | 289.23 | 248.11 | 218.64 | 269.32 | 270.70 | 267.91 |
| | Summer | 416.82 | 410.35 | 376.94 | 284.89 | 357.71 | 326.85 | 389.55 |
| | Autumn | 267.05 | 281.34 | 264.48 | 212.60 | 279.36 | 288.38 | 270.04 |
| $SW\downarrow_{toa}$ | Winter | 88.09 | 101.36 | 76.93 | 31.12 | 59.41 | 38.78 | 80.69 |
| | Spring | 660.78 | 679.40 | 629.79 | 533.62 | 581.03 | 525.12 | 638.74 |
| | Summer | 870.06 | 879.71 | 836.94 | 753.14 | 795.56 | 745.23 | 847.51 |
| | Autumn | 291.18 | 299.21 | 259.57 | 181.60 | 226.81 | 184.50 | 270.47 |
| $SW\uparrow_{toa}$ | Winter | 67.84 | 73.25 | 64.78 | 29.21 | 45.96 | 31.87 | 60.50 |
| | Spring | 356.97 | 327.56 | 390.42 | 388.70 | 322.22 | 298.02 | 347.20 |
| | Summer | 264.18 | 289.10 | 283.74 | 488.42 | 310.06 | 312.61 | 307.43 |
| | Autumn | 140.05 | 143.38 | 135.92 | 131.13 | 116.70 | 93.76 | 140.36 |
| $LW\uparrow_{toa}$ | Winter | 166.72 | 179.28 | 167.46 | 158.75 | 176.59 | 181.23 | 171.79 |
| | Spring | 198.34 | 205.80 | 194.30 | 179.70 | 197.16 | 196.08 | 198.28 |
| | Summer | 242.25 | 236.06 | 236.47 | 213.31 | 231.16 | 226.36 | 236.11 |
| | Autumn | 198.42 | 202.73 | 200.46 | 179.10 | 201.90 | 204.05 | 199.69 |
| $CF_S$ | Winter | −1.78 | −6.69 | −1.29 | −0.28 | −5.48 | −7.42 | −3.48 |
| | Spring | −24.61 | −48.32 | −6.18 | −2.22 | −45.12 | −54.26 | −35.68 |
| | Summer | −84.60 | −103.28 | −59.69 | −10.96 | −111.50 | −141.65 | −80.39 |
| | Autumn | −31.80 | −38.51 | −22.71 | −2.80 | −36.00 | −41.29 | −30.53 |
| $CF_L$ | Winter | 13.95 | 24.70 | 12.83 | 18.77 | 28.84 | 38.05 | 19.33 |
| | Spring | 20.16 | 29.15 | 11.42 | 6.29 | 28.39 | 33.52 | 23.11 |
| | Summer | 30.45 | 35.61 | 30.81 | 17.31 | 41.43 | 51.44 | 31.11 |
| | Autumn | 30.27 | 35.58 | 28.75 | 14.41 | 41.90 | 51.19 | 32.31 |
| $A_c$ | Winter | 0.49 | 0.58 | 0.48 | 0.56 | 0.64 | 0.74 | 0.54 |
| | Spring | 0.54 | 0.66 | 0.49 | 0.36 | 0.61 | 0.66 | 0.56 |
| | Summer | 0.65 | 0.71 | 0.67 | 0.56 | 0.74 | 0.81 | 0.66 |
| | Autumn | 0.62 | 0.67 | 0.62 | 0.49 | 0.72 | 0.81 | 0.63 |

[a] PID: parameter identification.
[b] The regions represented by region ID numbers 1 to 21 in this table can be found in Table 3. In addition, region 19 is the Arctic north of 60°N, region 20 is the Arctic Ocean north of 60°N, and region 21 represents the Arctic landmasses north of 60°N.
[c] The missing value is represented by 9999.00.

physical meanings of the 18 parameters are listed in Table 4.

### *b. Surface broadband albedo*

In situ measurements of surface broadband albedo are sparse, particularly over the Arctic Ocean. Most studies report results for individual stations or as regional results (cf. Serreze et al. 1998). Satellite data therefore play an important role in assessing the climatology of this parameter. Surface reflectance can be specified as "inherent" albedo or "apparent" albedo. The inherent albedo is the "true," no-atmosphere, or "black-sky" albedo of the surface, which is independent of the changes in the atmospheric conditions. The ap-

TABLE 3. Arctic region identification numbers and names.

| Region ID number | Region name |
|---|---|
| 1 | Beaufort Sea |
| 2 | Chukchi Sea |
| 3 | Canada Basin |
| 4 | Central Arctic |
| 5 | Laptev Sea |
| 6 | North Pole |
| 7 | Nansen Basin |
| 8 | Barents and Kara Seas |
| 9 | GIN Seas |
| 10 | Baffin Bay |
| 11 | Canada Archipelago Seas |
| 12 | Hudson Bay |
| 13 | North Europe |
| 14 | North-central Russia |
| 15 | Northeastern Russia |
| 16 | Alaska region |
| 17 | North Canada |
| 18 | Greenland |
| 19 | Arctic region north of 60°N |
| 20 | Arctic Ocean north of 60°N |
| 21 | Arctic landmasses north of 60°N |

TABLE 4. List of the names and physical meanings of the 18 retrieved climate parameters.

| PID name | Physical meaning |
|---|---|
| $T_s$ | Surface temperature (°C or K) |
| $\alpha_s$ | Broadband albedo [range: (0, 1)] |
| $R_e$ | Cloud droplet effective radius ($\mu$m) |
| $\tau_c$ | Cloud optical depth (unitless) |
| $\phi_c$ | Cloud particle phase (0 = liquid; 1 = ice) |
| $T_c$ | Cloud-top temperature (°C or K) |
| $P_c$ | Cloud-top pressure (hPa) |
| PW | Precipitable water (cm) |
| $SW\downarrow_{srf}$ | Downwelling shortwave radiation at the surface (W $m^{-2}$) |
| $LW\downarrow_{srf}$ | Downwelling longwave radiation at the surface (W $m^{-2}$) |
| $SW\uparrow_{srf}$ | Upwelling shortwave radiation at the surface (W $m^{-2}$) |
| $LW\uparrow_{srf}$ | Upwelling longwave radiation at the surface (W $m^{-2}$) |
| $SW\downarrow_{toa}$ | Downwelling shortwave radiation at the TOA (W $m^{-2}$) |
| $SW\uparrow_{toa}$ | Upwelling shortwave radiation at the TOA (W $m^{-2}$) |
| $LW\uparrow_{toa}$ | Upwelling longwave radiation at the TOA (W $m^{-2}$) |
| $CF_S$ | Shortwave cloud forcing at the surface (W $m^{-2}$) |
| $CF_L$ | Longwave cloud forcing at the surface (W $m^{-2}$) |
| $A_c$ | Cloud fraction (0–1, unitless) |

parent albedo is what would be measured by up- and down-looking radiometers and varies with the atmospheric conditions. Both vary with solar zenith angle and are directional in that regard. The APP-x dataset provides the directional–hemispheric apparent albedo.

Unlike the surface temperature, there are two peaks in the annual cycle of the surface albedo for the Arctic region north of 60°N: one in the early spring (about 60%) and the other in autumn (about 35%) as shown in Fig. 3b. The relatively low wintertime albedo corresponds to the low-latitude regions with less snow/ice coverage, because the dark, high-latitude areas are excluded from the statistics. The autumn peak is due to freeze-up, but more open water areas in autumn result in a lower albedo than in spring. Over the Arctic Ocean, the spring maximum surface albedo is about 60%, but the autumn second maximum albedo is only about 23%. For the Arctic landmasses north of 60°N, the autumn second maximum albedo is much higher than that for the Arctic seas and the entire Arctic region, with a value of approximately 45%. The Arctic annual mean surface albedo has a spatial distribution similar to surface temperature. The largest surface albedo is always in Greenland with a maximum value of as large as 90% throughout all seasons.

### *c. Cloud microphysical properties*

Clouds affect climate by interacting with the atmosphere and underlying surface through the absorption, emission, and scattering of radiation (Curry et al. 1996). Our knowledge of the spatial distribution of the Arctic clouds is based on a sparse record of the surface observations. Hahn (1995) reprocessed surface-based cloud fraction and corrected it for the biases introduced by darkness and fog for the period of 1982–91 for the Arctic region north of 80°N. Schweiger et al. (1999) used the NP drifting station data, a surface-based climatology, the ISCCP cloud product, and the TOVS Path-P data to assess similarities and differences in cloud cover datasets. Except for limited field experiments such as SHEBA, there are no datasets of cloud microphysical properties.

#### 1) CLOUD FRACTION

Cloud cover (cloud fraction) is defined as a percentage (proportion) of the sky covered by clouds. In the case of multilayer clouds, surface observations can only reflect low-layer cloudiness, though in the case of thin and low clouds, high cloud amount may be reported. For satellite observations of multilayered clouds, high clouds are observed most readily and low clouds are detected only when high clouds are thin.

Figure 5a shows that in an annual cycle over the entire Arctic, cloud cover is at its maximum in summer (75%). Wintertime cloud fraction is about 65%, and the least cloud coverage time of a year is spring, with an

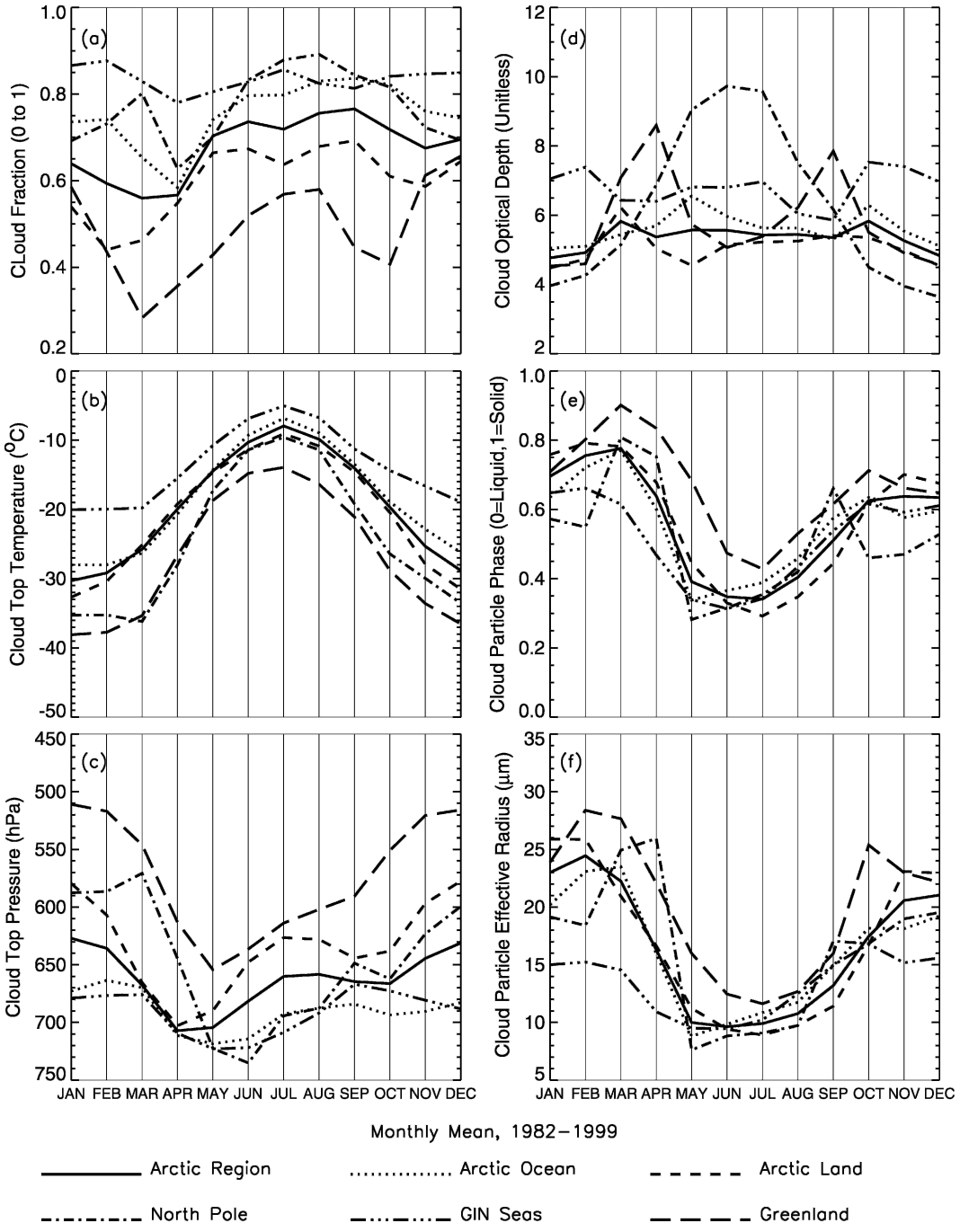


FIG. 5. Annual cycles of (a) cloud fraction, (b) cloud-top temperature, (c) cloud-top pressure, (d) cloud optical depth, (e) cloud particle phase, and (f) cloud particle effective radius for six Arctic regions averaged over the period 1982–99 on a local solar time of 14:00.

April value of about 55%. The similar temporal pattern of cloudiness also occurs for the Arctic Ocean and landmasses. The reasons why there are more clouds in summer than in winter were discussed by Curry et al. (1996) and Beeley and Moritz (1999). They noted that clear-sky ice crystal precipitation is a key factor causing lower cloudiness in winter due to the temperature-dependent formation, precipitation of the atmospheric ice, and low atmospheric humidity. But the reason for the lowest cloudiness in the transition seasons is unknown.

Spatially, the largest annual mean cloud cover occurs in the GIN and Barents Seas with a value of approxi-

mately 80%, and the lowest cloud cover occurs in central Greenland with a value of about 45%. The central Arctic Ocean has a cloud fraction of about 70%, and the landmasses have a cloud fraction of about 60%. In winter the cloud fraction over the GIN Seas tends to be greater than the annual average, reaching about 85%. Northern Canada and Siberia tend to have the lowest cloud coverage of about 45%, and the cloud fraction over Greenland is around 50%. In summer the largest cloud coverage occurs over the central Arctic rather than the GIN Seas, and the Arctic landmasses gain about 20% (absolute) more cloudiness than in winter. In spring, cloudiness over Greenland decreases to 30% from 50% in winter, and there is a 10% decrease of cloudiness over most of the central Arctic region, northern Canada archipelago, and Siberia. The spatial pattern of the cloudiness in autumn is similar to the annual mean pattern.

#### 2) CLOUD-TOP TEMPERATURE AND PRESSURE

Cloud-top temperature from satellite refers to cloud-radiating temperature and corresponds to the temperature somewhere beneath cloud top, generally within an optical depth of 1 from cloud top. Not surprisingly, the annual cycle of the cloud temperature follows the surface temperature pattern, though different in magnitude. The cloud-top temperature is uniformly lower than the surface temperature in all seasons over the entire Arctic region, the Arctic Ocean, and the Arctic landmasses poleward of 60°N. In winter the Arctic cloud temperature is generally 5°C lower than the surface temperature, but in summer the temperature difference can be as large as 20°C. The difference between the cloud temperature and the surface temperature is about 10°C for the Arctic Ocean all the year round, while for the Arctic landmasses the difference is much larger in summer (up to ~30°C) than in winter (~1°–2°C)as shown in Fig. 3a and Fig. 5b. Regardless of the season Greenland always has the lowest cloud temperature, with an annual mean of about –25°C, and most of the other Arctic regions have cloud temperatures of about –20°C, except the GIN Seas where the cloud temperature averages about –15°C. The cloud temperature is generally 10°C lower in winter than the annual mean, about the same in spring and autumn, and 10°C higher in summer (not shown).

Cloud-top pressure is, of course, directly related to cloud temperature and therefore has a similar cycle. Figure 5c shows that there are more high clouds in winter than in summer, and spring has more low clouds than other seasons. Clouds over the landmasses tend to be higher than those over the Arctic Ocean except in spring when the altitudes are similar, around 700 hPa. Spatially, clouds over Greenland are the highest by virtue of its elevation. Temporally, summertime clouds over Greenland tend to be lower than at other times of a year.

#### 3) CLOUD OPTICAL DEPTH

Cloud visible, vertical optical depth is a measure of the cumulative depletion of shortwave radiation as it passes through the cloud. It can be calculated as

$$\tau(\lambda, \theta) = \int_{Z_{\text{base}}}^{Z_{\text{top}}} \beta(\lambda, \theta, z)\, dz, \tag{1}$$

where $\beta$ is cloud volume extinction coefficient, $\lambda$ is radiation wavelength, $\theta$ is scattering angle, $z$ is the altitude within the cloud, and the integration is from cloud base $Z_{\text{base}}$ to the top $Z_{\text{top}}$. Optical depth is proportional to cloud physical thickness and is a function of cloud particle phase and size distribution. Cloud transmissivity is exponentially related to cloud optical depth, where an optical depth of 1 implies a transmissivity of 0.37. Unfortunately, cloud optical and microphysical properties are difficult to measure remotely, and there are no long-term datasets of these parameters.

As shown in Fig. 5d, cloud optical depth over the entire Arctic and the Arctic landmasses is the largest in transition seasons, that is, March and October when the cloud fraction is minimum, which may be related to more cyclone activity at those times (Key and Chan 1999). For the Arctic Ocean, the maximum cloud optical depth (thicker clouds) shifts to May. However, it should be noted that cloud optical depth retrievals have the highest uncertainty over bright surfaces at low sun angles, the predominant conditions during spring and fall. Less water vapor in the atmosphere, cold underlying surface, and more ice clouds produce the minimum cloud optical depth in winter.

Clouds are thicker in the GIN and Barents Seas and poleward to the North Pole on an annual time scale (not shown) than other regions. The thickest clouds occur in the east part of Greenland with values of about 8 to 9 (transmissivities of 0.000 12 to 0.000 34). Those regions with thicker clouds are associated with water vapor inflow through the GIN Seas from the North Atlantic. The spatial distribution patterns of cloud optical depth in the Arctic are variable both in season and in magnitude.

It should be noted that the daytime and nighttime algorithms for cloud optical depth, effective radius, and thermodynamic phase are conceptually similar but spectrally different. One difference is that the nighttime algorithm has an upper limit in optical depth of about 15–20, so optical depths larger than 15 are assigned this

maximum value. Unfortunately, determining how consistent the daytime and nighttime algorithms are is not straightforward because one channel used by both algorithms (3.7 microns) is used in a very different way in the presence of sunlight. Further validation with in situ data is needed.

#### 4) Cloud particle phase and effective radius

In the APP-x retrievals, all clouds are composed of either liquid droplets ("water cloud") or solid ice crystals ("ice cloud"). Cloud optical properties are closely related to cloud particle phase, shape (for ice), and size distribution. Cloud particle effective radius $R_e$ for liquid droplets is a ratio of the third to second moments of cloud drop size distribution $N(r)$

$$R_e = \frac{\int_0^\infty r^3 \cdot N(r)\, dr}{\int_0^\infty r^2 \cdot N(r)\, dr}, \tag{2}$$

where $N(r) = \int_{Z_{\text{base}}}^{Z_{\text{top}}} n(r, z)\, dz$, $n(r, z)$ is the size distribution at the altitude $z$.

Ice crystal optical properties are based on the parameterization of Key et al. (2002). The effective radius is half of the effective size, defined as

$$R_e = \frac{3}{4} \frac{\sum_{L=L_{\min}}^{L=L_{\max}} V(L) n(L) \Delta L}{\sum_{L=L_{\min}}^{L=L_{\max}} A(L) n(L) \Delta L}, \tag{3}$$

where $L$ is the maximum dimension of an ice crystal, $n(L)$ is the number of particles with maximum dimension $L$ in the size distribution, $\Delta L$ is the width of a size bin, and $V$ and $A$ are the volume and total projected area of the ice crystals, respectively.

Over the annual cycle, about 70% of the clouds are in solid ice phase over the entire Arctic region in winter, while in summer liquid clouds make up about 70% of the clouds (Fig. 5e). In general, ice clouds tend to have larger particles than liquid clouds; thus it should be no surprise to see that the annual fluctuation of cloud particle effective radius follows the curve of cloud particle phase (Fig. 5f). It is worth pointing out that over the Arctic Ocean the minimum cloud particle sizes occur in late spring (May) in correspondence with the highest frequency of liquid clouds rather than in summer when the landmasses have the most liquid clouds. Most ice clouds and maximum cloud particle sizes do not occur in the coldest month but rather in early spring (March) over the Arctic Ocean.

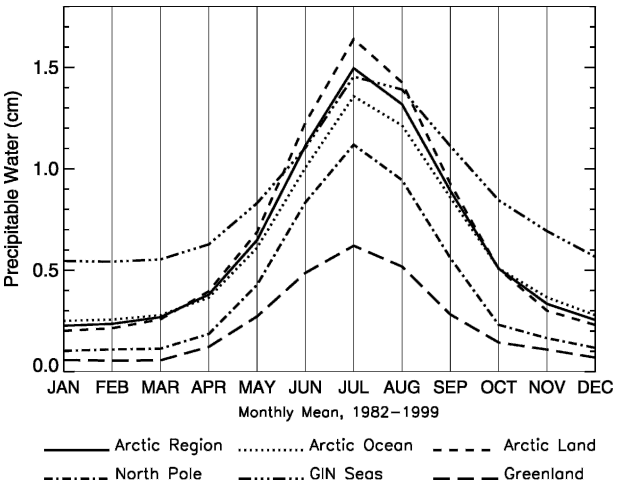


FIG. 6. Same as in Fig. 3, but for PW.

As expected, Greenland has much more ice clouds and larger cloud particle sizes than other Arctic regions on annual average. In winter more ice clouds occur over the Arctic landmasses than the Arctic Ocean, with the particle sizes as large as 30 $\mu$m. Summertime clouds are predominantly liquid and are equally distributed over the landmass and ocean regions with the average particle size of 10 $\mu$m.

### d. Precipitable water

In this study, precipitable water (PW) data were obtained directly from the NCEP–NCAR reanalysis with spatial resolution of 2.5° × 2.5° latitude–longitude and were interpolated to APP-x 25 × 25 km$^2$ spatial resolution grid. The annual cycle of PW follows the surface temperature, that is, the largest PW (~1.5 cm) occurs in summer and the lowest PW (~0.2 cm) in winter (Fig. 6). Precipitable water is the lowest over Greenland all year round with an annual mean value of about 0.2 cm, and the GIN Seas have the largest PW (~1.0 cm) due to moisture transport from the North Atlantic.

### e. Radiation

Very few studies have been performed on the Arctic surface radiation field. Serreze et al. (1998) studied monthly climatology of the global radiation (downwelling solar radiation) for the Arctic with the measurements from the Russian North Pole series of drifting stations, the United States drifting stations "T-3," and "Arlis II" land stations. This section will discuss the radiation fields across the Arctic from the APP-x dataset.

Figure 7 shows the annual cycle of downwelling shortwave and longwave radiative fluxes at the surface on a local solar time of 14:00. As expected, the largest downwelling shortwave radiative flux occurs in June, while the largest downwelling and upwelling longwave radiative fluxes (not shown) as well as the net all-wave radiative flux occur one month later, that is, in July. Another feature is that the largest upwelling shortwave flux (not shown) occurs in May rather than in June because relatively higher surface albedo in May reflects more downwelling shortwave radiation than that in June, though the larger downwelling shortwave radiation occurs in June.

Regarding the net shortwave, net longwave, and net all-wave radiative fluxes at the surface, one feature is that the largest loss of the longwave radiative energy from the surface occurs in April, corresponding to the lowest cloud fraction and hence the lowest downwelling longwave flux at that time. The net all-wave radiation follows the net shortwave radiation, though lower in magnitude. For the landmasses, the greatest loss of longwave radiation is in July due to the high surface temperature.

The spatial distribution of the annual mean net all-wave radiative fluxes at the surface (not shown) exhibits its minimum net radiative fluxes in the central Arctic Ocean and Greenland. For the net longwave radiative fluxes at the surface, the loss of the longwave radiation to the atmosphere is mainly from the Arctic landmasses, as shown in Fig. 8.

The annual cycle of the net shortwave, longwave, and all-wave radiative fluxes at the top of the atmosphere (TOA) is shown in Fig. 9. As expected, the earth–atmosphere system gains radiative energy in summer and loses radiative energy in winter. On annual average, the Arctic region north of about 70°N loses radiative energy to space, acting as a heat sink.

### *f. Cloud radiative effect*

Clouds attenuate sunlight, causing a decrease in the downwelling shortwave radiation at the surface during the daytime. Clouds also emit infrared radiation to the surface, resulting in a greater downwelling longwave flux than in clear conditions. Therefore clouds have a cooling effect on the surface in the shortwave, but a warming effect in terms of infrared radiation. Overall the effect of clouds on the radiation budget depends on the balance between shortwave and longwave budgets affected by clouds. The cloud radiative effect is also commonly called cloud forcing. Cloud forcing (CF) is calculated from net shortwave and longwave radiative fluxes at the surface and TOA. It is defined as

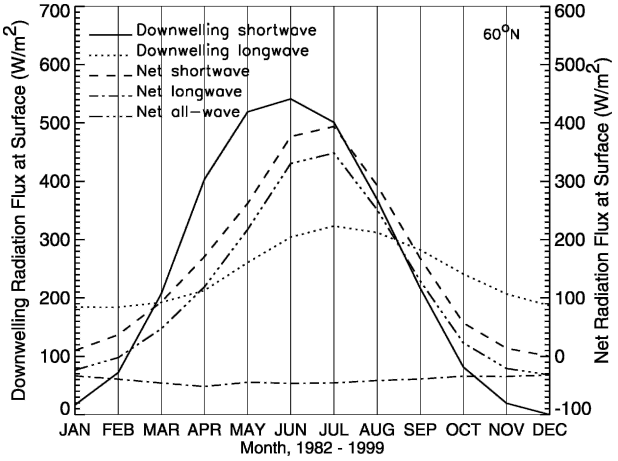


FIG. 7. Annual cycles of downwelling shortwave, longwave, and net radiative fluxes at the surface averaged over the period 1982–99 on a local solar time of 14:00 for the Arctic region north of 60°N.

$$\mathrm{CF}_{\lambda,z} = \int_0^{A_c} \frac{\partial F_{\lambda,z}}{\partial a}\, da = F_{\lambda,z}(A_c) - F_{\lambda,z}(0), \qquad (4)$$

where $F_{\lambda,z}$ is the net flux (W m$^{-2}$) in shortwave or longwave radiation at the surface or TOA, $\lambda$ is the wavelength, $z$ is the altitude above the surface, and $A_c$ is the cloud fraction in the scene. The net flux is equal to the downwelling minus upwelling fluxes. The all-wave cloud forcing can be calculated by

$$\mathrm{CF}_z = \mathrm{CF}_{\mathrm{shortwave}} + \mathrm{CF}_{\mathrm{longwave}}. \qquad (5)$$

Cloud forcing is also influenced by surface and atmospheric conditions such as surface albedo and atmospheric profile. For example, the shortwave cloud forcing will become more negative as surface albedo decreases, even with no change in cloud properties.

Figure 10 shows the annual cycle of the shortwave, longwave, and all-wave cloud forcing at the surface. As discussed above, the shortwave cloud forcing is always negative, while the longwave cloud forcing is always positive and follows the annual cycle of cloud fraction. In cold season (October–March) the all-wave cloud forcing is positive, implying a warming effect of the clouds on the surface, while in warm season (April–September) the all-wave cloud forcing is negative, indicating a cooling effect of the clouds on the surface. On annual average, clouds have a warming effect over Greenland, the North Pole (north of 80°N), the northern Canada Archipelago, the Beaufort and Chukchi Seas, and most of the Laptev Sea as shown partly in Fig. 11. In winter clouds have a warming effect on the surface almost everywhere over the Arctic region north of 60°N, but in summer the cloud warming effect only

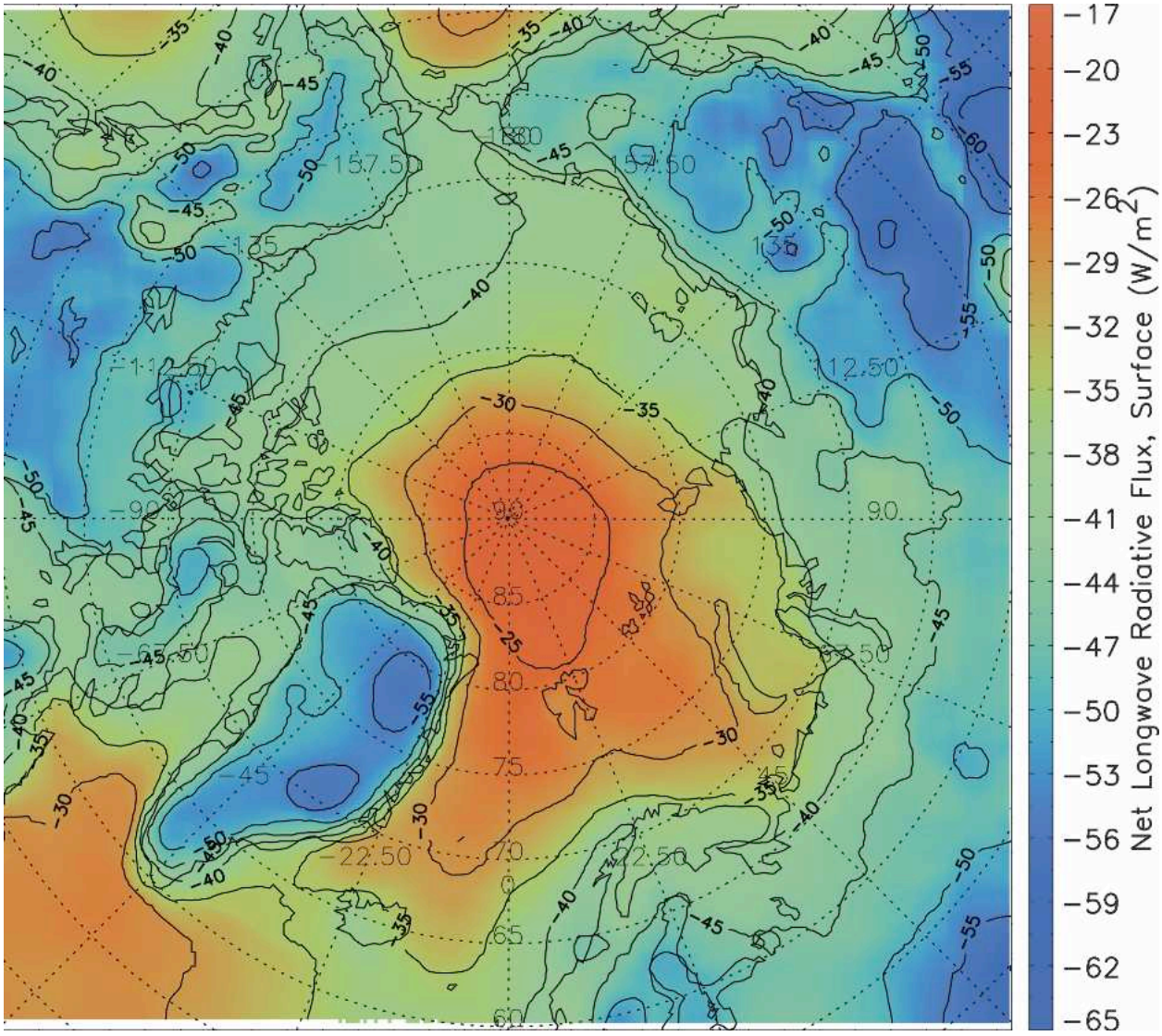


FIG. 8. Same as in Fig. 4, but for annual mean net longwave radiative fluxes at the surface.

holds for Greenland and the western part of the central Arctic region as a result of the high surface albedo.

## 4. Summary and conclusions

Over the annual cycle, the Arctic surface temperature varies most for the landmasses and least for the Arctic Ocean. Greenland is the coldest part of the Arctic by virtue of its altitude, with an average surface temperature of –40°C in winter. The average maximum surface temperature of about 20°C occurs during summer in northeastern Russia. The Arctic surface albedo has a maximum value of as large as 90% in the center of Greenland and a minimum value of less than 5% in the GIN Seas during summer. NCEP–NCAR reanalysis data show that atmospheric precipitable water is extremely low in winter at about 0.2 cm and increases to about 1.5 cm in summer.

The Arctic is one of the cloudiest regions on the earth. The annual mean cloud coverage is about 70%. The maximum monthly cloudiness occurs in September at about 75%, and the minimum occurs in April at about 55%. Spatially, Greenland is the least cloudy area of the Arctic, and the GIN seas are the cloudiest. As expected, about 70% of the clouds are in solid phase (ice) in winter, and about the same proportions of the clouds are in liquid phase in summer. Most ice clouds and clouds with large cloud particle sizes do not occur in the coldest month but rather in early spring (March) over the Arctic Ocean. In general, visible cloud optical

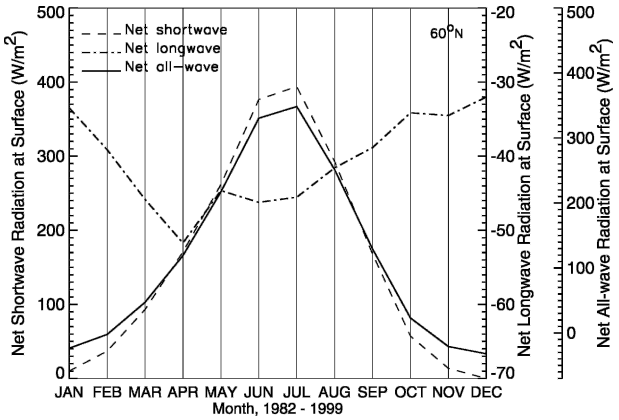


FIG. 9. Annual cycle of all components of net radiation field at the TOA averaged over the period 1982–99 on a local solar time of 14:00 for the Arctic region north of 60°N.

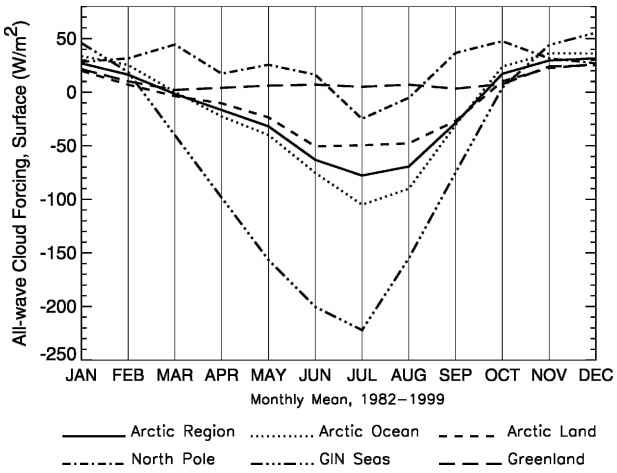


FIG. 11. Same as in Fig. 3, but for net all-wave cloud forcing.

depth is about 5 ~ 6 for the Arctic overall. Optically thick clouds occur in transition seasons for every region in the Arctic except the GIN Seas where thick clouds occur in summer. The Arctic cloud-top temperature basically follows the surface temperature variation in space and time. Overall, the cloud temperature is lower than the surface temperature; the difference between them is about 5°C in winter and can be as large as 20°C in summer because of the frequent temperature inversions and less water vapor in winter. In general, Arctic clouds exist at pressure levels of ~750–600 hPa except over Greenland where the cloud top pressure is usually between ~600 and 450 hPa.

In winter, clouds have a warming effect on the surface almost everywhere in the Arctic north of 60°N, but in summer clouds warm the surface only over Greenland and the western part of the central Arctic. The largest downwelling shortwave radiation occurs in June at the surface, while the largest downwelling and upwelling longwave radiation, as well as the net all-wave radiation, occurs one month later in July. The largest upwelling shortwave radiation occurs in May rather than in June. The largest loss of the longwave radiative energy from the surface to the atmosphere occurs in April, corresponding to the lowest cloud coverage in the same month. In addition, even though this study used the data acquired at high sun time, it is also evident that on annual average, the Arctic north of about 70°N loses radiative energy to space, acting as a heat sink.

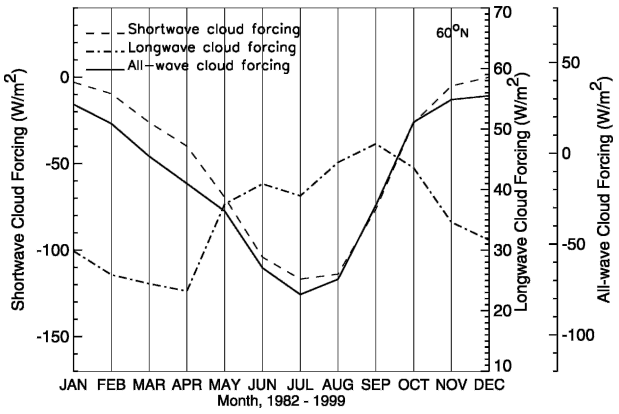


FIG. 10. Same as in Fig. 9, but for shortwave, longwave, and all-wave cloud forcing at the surface.

*Acknowledgments.* This work was supported by the National Oceanic and Atmospheric Administration (NOAA) Arctic Research Office and the National Science Foundation (NSF; Grants OPP-0240827 and OPP-0230317). We thank C. Fowler, J. Maslanik, T. Scambos, and T. Haran for their work on the AVHRR Polar Pathfinder dataset. The National Snow and Ice Data Center (NSIDC) provided the standard APP dataset. The NCEP–NCAR reanalysis global profile dataset was provided by the NOAA–CIRES Climate Diagnostics Center. The NASA Langley Research Center provided the ISCCP D2 ozone dataset. Thanks also go to the two anonymous reviewers for their helpful comments and suggestions. The views, opinions, and findings contained in this report are those of the author(s) and should not be construed as an official National Oceanic and Atmospheric Administration or U.S. Government position, policy, or decision.

## REFERENCES

Barry, R. G., M. C. Serreze, J. A. Maslanik, and R. H. Preller, 1993: The Arctic Sea ice-climate system: Observations and modeling. *Rev. Geophys.,* **31,** 397–422.

Beesley, J. A., and R. E. Moritz, 1999: Toward an explanation of the annual cycle of cloudiness over the Arctic Ocean. *J. Climate,* **12,** 395–415.

Cavalieri, D. J., C. L. Parkinson, P. Gloersen, J. C. Comiso, and H. J. Zwally, 1999: Deriving long-term time series of sea ice cover from satellite passive-microwave multisensor data sets. *J. Geophys. Res.,* **104,** 15 803–15 814.

Curry, J. A., and E. E. Ebert, 1992: Annual cycle of radiative fluxes over the Arctic Ocean: Sensitivity to cloud optical properties. *J. Climate,* **5,** 1267–1280.

——, W. B. Rossow, D. Randall, and J. L. Schramm, 1996: Overview of Arctic cloud and radiation characteristics. *J. Climate,* **9,** 1731–1764.

Drobot, S., and M. Anderson, 2001; Snow melt onset over Arctic Sea ice from SMMR and SSM/I brightness temperatures. National Snow and Ice Data Center, Boulder, CO. [Available online at http://nsidc.org/data/docs/daac/nsidc0105_arctic_snowmelt_onset_dates.gd.html.]

Fowler, C., J. Maslanik, T. Haran, T. Scambos, J. Key, and W. Emery, 2000: AVHRR Polar Pathfinder twice-daily 5 km EASE-grid composites. National Snow and Ice Data Center, Boulder, CO. [Available online at http://nsidc.org/data/docs/daac/nsidc0066_avhrr_5km.gd.html.]

Francis, J. A., and A. J. Schweiger, 1999: The NASA/NOAA TOVS Polar Pathfinder: 18 years of Arctic data. Preprints, *Fifth Conference on Polar Meteorology and Oceanography,* Dallas, TX, Amer. Meteor. Soc., 62–65.

Groves, D. G., and J. A. Francis, 2002: Variability of the Arctic atmosphere moisture budget from TOVS satellite data. *J. Geophys. Res.,* **107,** 4785, doi:10.1029/2002JD002285.

Gultepe, I., G. Isaac, J. Key, T. Uttal, J. Intrieri, D. Starr, and K. Strawbridge, 2004: Dynamical and microphysical characteristics of Arctic clouds using integrated observations collected over SHEBA during the April 1998 FIRE-ACE flights of the Canadian Convair. *Meteor. Atmos. Phys.,* **85,** 235–263.

Hahn, C., 1995: The effect of moonlight on observation of cloud cover at night, and application to cloud climatology. *J. Climate,* **8,** 1429–1446.

Key, J. R., 2002a: The cloud and surface parameter retrieval (CASPR) system for polar AVHRR. Cooperative Institute for Meteorological Satellite Studies, University of Wisconsin—Madison, 59 pp. [Available online at http://stratus.ssec.wisc.edu/caspr/documentation.html.]

——, 2002b: Streamer user's guide. Cooperative Institute for Meteorological Satellite Studies, University of Wisconsin—Madison, 107 pp. [Available online at http://stratus.ssec.wisc.edu/streamer/documentation.html.]

——, and A. J. Schweiger, 1998: Tools for atmospheric radiative transfer: Streamer and FluxNet. *Comput. Geosci.,* **24,** 443–451.

——, and A. C. K. Chan, 1999: Multidecadal global and regional trends in 1000 mb and 500 mb cyclone frequencies. *Geophys. Res. Lett.,* **26,** 2053–2056.

——, and J. Intrieri, 2000: Cloud particle phase determination with the AVHRR. *J. Appl. Meteor.,* **39,** 1797–1805.

——, A. J. Schweiger, and R. S. Stone, 1997: Expected uncertainty in satellite-derived estimates of the high-latitude surface radiation budget. *J. Geophys. Res.,* **102** (C7), 15 837–15 847.

——, X. Wang, J. C. Stroeve, and C. Fowler, 2001: Estimating the cloudy sky albedo of sea ice and snow from space. *J. Geophys. Res.,* **106** (D12), 12 489–12 497.

——, P. Yang, B. Baum, and S. Nasiri, 2002: Parameterization of shortwave ice cloud optical properties for various particle habits. *J. Geophys. Res.,* **107,** 4181, doi:10.1029/2001JD000742.

Manabe, S., and R. J. Stouffer, 1994: Multiple-century response of a coupled ocean–atmosphere model to an increase of atmospheric carbon dioxide. *J. Climate,* **7,** 5–23.

——, M. J. Spelman, and R. J. Stouffer, 1992: Transient response of a coupled ocean–atmosphere model to gradual changes of atmospheric $CO_2$. Part II: Seasonal response. *J. Climate,* **5,** 105–126.

Martin, S. E., and E. Munoz, 1997: Properties of the Arctic 2-m air temperature for 1979–present derived from a new gridded dataset. *J. Climate,* **10,** 1428–1440.

——, ——, and R. Drucker, 1997: Recent observations of a Spring-Summer warming over the Arctic Ocean. *Geophys. Res. Lett.,* **24,** 1259–1262.

Maslanik, J. A., J. R. Key, C. W. Fowler, T. Nguyen, and X. Wang, 2001: Spatial and temporal variability of satellite-derived cloud and surface characteristics during FIRE-ACE. *J. Geophys. Res.,* **106** (D14), 15 233–15 249.

Meehl, G. A., and W. M. Washington, 1990: $CO_2$ climate sensitivity and snow-sea-ice parameterization in an atmospheric GCM coupled to a mixed-layer ocean model. *Climate Change,* **16,** 283–306.

Meier, W., J. A. Maslanik, J. R. Key, and C. W. Fowler, 1997: Multiparameter AVHRR-derived products for Arctic climate studies. *Earth Interactions*, **1**. [Available online at http://EarthInteractions.org.]

Miller, J. R., and G. L. Russell, 2000: Projected impact of climatic change on the freshwater and salt budgets of the Arctic Ocean by a GCM. *Geophys. Res. Lett.,* **27,** 1183–1186.

Pavolonis, M. J., and J. R., Key, 2003: Antarctic cloud radiative forcing at the surface estimated from the ISCCP D2 and AVHRR polar pathfinder data sets, 1985–1993. *J. Appl. Meteor.,* **42,** 827–840.

Rossow, W. B., A. W. Walker, D. E. Beuschel, and M. D. Roiter, 1996: International satellite cloud climatology project (ISCCP) documentation of new cloud datasets. WMO/TD 737, World Meteorological Organization, 115 pp. [Available online at http://isccp.giss.nasa.gov/docs/documents.html.]

Schweiger, A. J., R. W. Lindsay, J. R. Key, and J. A. Francis, 1999: Arctic cloud in multiyear satellite data set. *Geophys. Res. Lett.,* **26,** 1845–1848.

Serreze, M. C., J. R. Key, J. E. Box, J. A. Maslanik, and K. Steffen, 1998: A new monthly climatology of global radiation for the Arctic and comparisons with NCEP–NCAR reanalysis and ISCCP-C2 fields. *J. Climate,* **11,** 121–136.

Stroeve, J., and Coauthors, 2000: Observational evidence of recent change in the northern high-latitude environment. *Climate Change ,* **46,** 159–207.

——, J. Box, C. Fowler, T. Haran, and J. R. Key, 2001: Intercomparison between in situ and AVHRR Polar Pathfinder-derived surface albedo over Greenland. *Remote Sens. Environ.,* **75,** 360–374.

Wang, X., and J. R. Key, 2003: Recent trends in Arctic surface, cloud, and radiation properties from space. *Science,* **299,** 1725–1728.

——, and ——, 2005: Arctic surface, cloud, and radiation properties based on the AVHRR Polar Pathfinder dataset. Part II: Recent trends. *J. Climate,* **18,** 2575–2593.